Numerical simulation with low artificial dissipation of transitional flow over a delta wing

Rozema, Wybe; Kok, Johan; Veldman, Arthur; Verstappen, R.W.C.P.

Published in:
Journal of computational physics

DOI:
10.1016/j.jcp.2019.109182

Publication date:
2020

Journal of Computational Physics 405 (2020) 109182

Contents lists available at ScienceDirect

Journal of Computational Physics

www.elsevier.com/locate/jcp

Numerical simulation with low artificial dissipation of transitional flow over a delta wing

Wybe Rozema [a,b], Johan C. Kok [b], Arthur E.P. Veldman [a,*], Roel W.C.P. Verstappen [a]

[a] Bernoulli Institute, University of Groningen, PO Box 407, 9700AK Groningen, the Netherlands
[b] Netherlands Aerospace Centre NLR, PO Box 90502, 1006BM Amsterdam, the Netherlands

ARTICLE INFO

Article history:
Received 4 April 2019
Received in revised form 20 September 2019
Accepted 9 December 2019
Available online 13 December 2019

Keywords:
Delta wing
CFD
Compressible flow
Laminar-turbulent transition
Energy-conserving discretization
Supra-conservative

ABSTRACT

A low-dissipation simulation method is used to perform simulations of transitional aerodynamic flow over a delta wing. For an accurate simulation of such a flow, numerical conservation of important physical quantities is desirable. In particular, the discretization of the convective terms of the Navier–Stokes equations should not spuriously generate or dissipate kinetic energy, because this can interfere with the transition to turbulent flow. Conservation of discrete kinetic energy by the discretized convective terms can be achieved by writing the Navier–Stokes equations in square-root variables, which results in a skew-symmetric convective term. In the paper, simulations with such a low-dissipation method are presented at chord Reynolds numbers around 200,000. The results show good agreement with experimental measurements.

1. Introduction

Although the Navier-Stokes equations for turbulent flow have been known since 1822, their numerical solution is still a formidable task. Roughly, the computational effort required for a detailed direct numerical simulation scales with the Reynolds number as $Re^{11/4}$, e.g. [1–3]. Yet, in spite of this high computational cost, accurate numerical simulation is currently feasible for flows at moderate Reynolds numbers.

For simulation of turbulent flow, the energy errors of the numerical method should not overwhelm the physical energy dissipation [4–6], because too much artificial dissipation can delay transition to turbulence of shear layers. Also, numerical energy dissipation can inadequately damp radiated acoustic waves [7,8].

This resulted in a quest for higher-order accurate central discretization methods with no or very limited numerical energy dissipation: so-called low-dissipation methods [9]. In this paper, such a numerical simulation method for compressible flow is presented. The method has good stability properties as it prevents spurious numerical generation or dissipation of energy. Therefore, addition of numerical dissipation to prevent instabilities related to spurious energy generation is not necessary. We will demonstrate that the method is capable of accurately predicting natural transition from laminar to turbulent flow for an application of engineering relevance.

* Corresponding author.
E-mail addresses: wyberozema@gmail.com (W. Rozema), johan.kok@nlr.nl (J.C. Kok), a.e.p.veldman@rug.nl (A.E.P. Veldman), r.w.c.p.verstappen@rug.nl (R.W.C.P. Verstappen).

https://doi.org/10.1016/j.jcp.2019.109182
0021-9991/

A key ingredient of the simulation method is discrete conservation of primary and secondary invariants. In particular, convection does not generate or dissipate kinetic energy. The favorable influence of these energy-preserving discretizations was already recognized half-way the 20th century by Phillips [10,11], Lilly [12], Arakawa [13] and Bryan [14], who were all interested in long-term numerical integration of meteorological flow. They recognized the influence of the discretization of the non-linear convective term on numerical stability (non-linear instability). A considerable step forward was made for incompressible flow through the introduction of the staggered-grid discretization by Harlow and Welch in the mid-1960s [15]. At that time, Richtmyer and Morton [16, p. 142] already noticed that some discretizations conserve an energy norm "thus ensuring stability". Piacsek and Williams [17] introduced the skew-symmetric form of the equations as a starting point for deriving a finite-difference discretization, which directly resulted in discrete energy conservation.

An energy-conserving discretization of the incompressible Navier–Stokes equations has been introduced by Morinishi [18], who discusses (higher-order) finite-difference discretization of the convective, divergence and skew-symmetric forms of the convective terms on uniform grids; see also [19,20]. Around the same time, finite-volume discretizations starting from conservation laws were developed, for which momentum conservation is preserved numerically by design. Inspired by [21], Verstappen and Veldman [22] combined discrete momentum and energy conservation for incompressible flow on staggered non-uniform Cartesian grids; higher-order versions followed soon [23,24]. Trias et al. [25–28] generalized the approach to unstructured (collocated and/or staggered) grids.

All these approaches are based on a skew-symmetric discretization of the conservative convective terms, which results in discrete energy conservation and numerical stability in a mathematically elegant way. A similar philosophy can be found in the closely related summation-by-parts (SBP) method, introduced by Strand and Olsson [29–31] and generalized in [32–34].

Early extensions to the equations for compressible flow have been presented using skew-symmetric formulations by Feiereisen et al. [35] and Blaisdell et al. [36]. Since the turn of the century, several numerical studies have been presented based on a finite-volume discretization of the conservative flow equations, for example by Ducros et al. [37], Jameson [38], Kok [8], Nordström et al. [39], Morinishi [40] and Rozema [41]. Also, similar energy-conserving methods have been developed for the shallow-water equations [42]. A more complete overview of the above numerical developments for aerodynamic flow is provided in the review paper on low-dissipation methods and models by Rozema et al. [9], and the review paper on energy-conserving methods by Coppola et al. [43].

In addition to conservative spatial discretizations, efforts have been made to derive conservative time integration methods. In particular, an energy conservative time integration for compressible flow appears to require the introduction of the square root of the density $\sqrt{\rho}$, as advocated in the proposals by Guermond and Quartapelle [44], Subbareddy and Candler [45], Morinishi [40] and Rozema [46]. In line with the use of these square-root variables in the time-integration method, spatial discretization studies were carried out based on these same variables by, e.g., Reiss et al. [47–49], Rozema et al. [50–52] and Cadieux et al. [53].

In this paper, which is based on the PhD thesis of the first author [52], we will follow a similar approach, in which the compressible Navier–Stokes equations will be reformulated in terms of square-root variables. In this way, a discretization method is developed for curvilinear grids which has a fourth-order local trunacation error in computational space. It not only conserves the primary variables mass, momentum and total energy, but also it convectively conserves the secondary variables kinetic and internal energy. Because the discretization has more conservation properties than a standard finite-volume discretization, it could be called *supra-conservative*. Moreover, in addition to the already mentioned symplectic time-integration property, the formulation allows for the development of regularization turbulence models [41,54]. However, such conservative time-integration methods and turbulence models will not be used for the simulations in this paper.

Previously, the energy-conserving simulation method for compressible flow has been used for large-eddy simulation of the flow over a delta wing, yet at a slightly smaller Reynolds number [55]. These simulations were numerically stable and gave physically accurate results. Following up on this work, we use the same discretization, but this time without turbulence model, i.e., in principle we perform a direct numerical simulation. A fourth-order energy-conserving method is used to perform accurate numerical simulations of the transitional aerodynamic flow over a delta wing at chord Reynolds numbers of $\mathrm{Re}_c = 150,000$ and $211,200$. The results obtained with this low-dissipation method are compared with experimental results by Riley and Lowson [56]. An impression of the vortical structures above the wing is given in Fig. 1, which shows the stream-wise development of the vorticity at $\mathrm{Re}_c = 150,000$.

Outline of the paper. The formulation of the equations for compressible flow is given in Sect. 2, together with some considerations on primary and secondary conservation. The supra-conservative discretization method for curvilinear grids is outlined in Sect. 3. Thereafter, Sect. 4 explains the physics of the flow past the delta wing, which is used as validation material for the numerical simulations presented in Sect. 6. In Sect. 5 the numerical method is verified through grid refinement.

2. The compressible Navier–Stokes equations

2.1. Primary conservation

Aerodynamics is governed by the Navier–Stokes equations for compressible flow:

$$\partial_t \rho + \nabla \cdot (\rho \mathbf{u}) = 0,$$

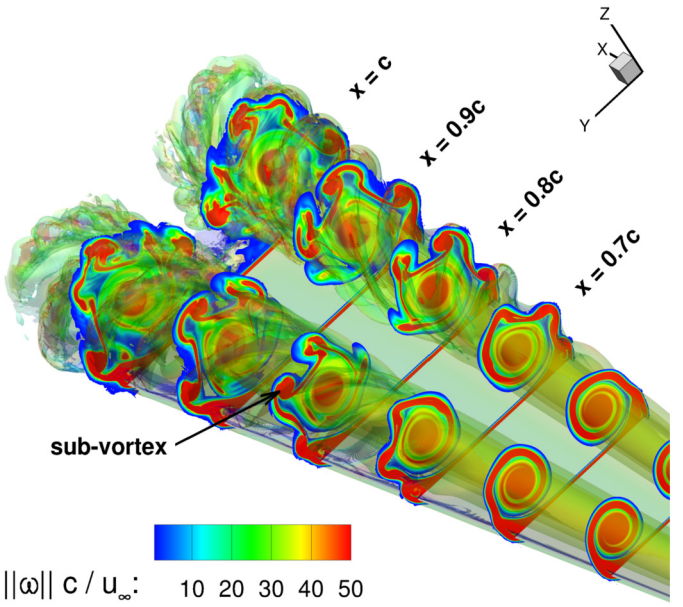

Fig. 1. Axial slices of the instantaneous vorticity magnitude for $\mathrm{Re}_c = 150,000$ computed on a fine computational grid.

$$\partial_t \rho \mathbf{u} + \nabla \cdot (\rho \mathbf{u} \otimes \mathbf{u}) + \nabla p = \nabla \cdot \sigma, \tag{1}$$
$$\partial_t \rho E + \nabla \cdot (\rho \mathbf{u} E) + \nabla \cdot (p\mathbf{u}) = \nabla \cdot (\sigma \cdot \mathbf{u}) - \nabla \cdot \mathbf{q}.$$

Here ρ is the mass density, $\mathbf{u}$ the flow velocity, $\rho E = \frac{1}{2}\rho \mathbf{u} \cdot \mathbf{u} + \rho e$ the total energy density, ρe the internal energy density, p the pressure, σ the tensor with viscous stresses, and $\mathbf{q}$ the heat diffusion flux.

The Navier–Stokes equations are closed by the standard thermodynamical relations for a perfect gas: $p = \rho R T$, relating pressure with temperature T while R is the gas constant, and $e = c_v T$, where e is the internal energy and c_v the specific heat at constant volume. The latter is related to the specific heat at constant pressure c_p by the ratio $\gamma \equiv c_p / c_v = 1.4$.

The viscous stress is closed by assuming that air is a Newtonian fluid

$$\sigma = 2\mu(T)\left(S - \tfrac{1}{3}\,\mathrm{tr}(S) I\right), \quad S_{ij} = \tfrac{1}{2}(\partial_i u_j + \partial_j u_i), \tag{2}$$

where $\mu(T)$ is the dynamic viscosity (Sutherland's law) and S is the symmetric rate-of-strain tensor. Heat diffusion is modeled with Fourier's law $\mathbf{q} = -k\nabla T$, where k is the thermal conductivity set by the Prandtl number $\mathrm{Pr} \equiv c_p \mu / k = 0.72$.

In Eq. (1), the Navier–Stokes equations have been expressed in conservative form. This form directly expresses conservation of mass, momentum, and total energy in a flow, because all the terms in the equations of motion are either in divergence or gradient form. Therefore they are called primary conservation laws.

2.2. Secondary conservation

The convective terms do not only conserve mass, momentum, and total energy, but also kinetic energy and internal energy separately. The latter property follows from a combination of the primary conservation laws. Ignoring the viscous terms, the evolution equation for the kinetic energy density follows as

$$\begin{aligned}\partial_t(\tfrac{1}{2}\rho \mathbf{u} \cdot \mathbf{u}) &= \mathbf{u} \cdot \partial_t(\rho \mathbf{u}) - \tfrac{1}{2}(\mathbf{u} \cdot \mathbf{u})\partial_t \rho \\ &= -\mathbf{u} \cdot \nabla \cdot (\rho \mathbf{u} \otimes \mathbf{u}) - \mathbf{u} \cdot \nabla p + \tfrac{1}{2}(\mathbf{u} \cdot \mathbf{u})\nabla \cdot (\rho \mathbf{u}) \\ &= -\nabla \cdot ((\tfrac{1}{2}\rho \mathbf{u} \cdot \mathbf{u})\mathbf{u}) - \nabla \cdot (p\mathbf{u}) + p(\nabla \cdot \mathbf{u}).\end{aligned}$$

The first term on the right-hand side, due to convection, has a divergence form, implying that kinetic energy is conserved by convective transport. As the total energy is also conserved by convection, it also conserves internal energy. The pressure terms conserve kinetic energy in the incompressible limit $\nabla \cdot \mathbf{u} = 0$, but through compression they are responsible for exchange between kinetic and internal energy. Convective conservation of kinetic and internal energy are important secondary conservation properties, and they will be preserved by the discretization that is developed in the next section.

3. Energy-preserving discretization

The energy-preserving spatial discretizations of the compressible Navier–Stokes equations to be derived in this section aim to preserve the conservation properties of

1. mass,
2. (linear) momentum,
3. kinetic energy,
4. internal energy, and (therefore)
5. total energy

at the discrete level. The choice of preserving these conservation properties is motivated by practical experience with simulations of (in)compressible flow. For instance, conservation of vorticity, entropy, helicity and/or enstrophy [57] can also be interesting, but is out of the scope of the present paper.

There exist, at least, two approaches to achieve the above discrete conservation properties. The traditional one is based on the familiar formulation in terms of the primitive variables. In the introduction above, a short overview of the many studies in this vein has already been given. A method of particular relevance for the current study is the one developed by Kok [8]. It conserves all the above-mentioned physical quantities, and was the first to be implemented in the NLR simulation suite Enflow. This approach has been used successfully, for example, for hybrid RaNS-LES simulations of compressible turbulent flow [58,59].

As mentioned in the introduction, an alternative approach is to derive a discretization using square-root variables. In fact, use of square-root variables allows for more desirable properties. Firstly, it is possible to define energy-preserving (symplectic) time integration methods, using the midpoint rule [45,40] or higher-order variants [44,47,48,53]. Secondly, it is possible to define symmetry-preserving regularization turbulence models [41,9]. As the current research originally started with the latter models for compressible turbulent flow, the explanation of the numerical discretization presented in this paper will be based on these square-root variables.

3.1. Square-root variables, skew symmetry and conservation of products

The primary and secondary conservation properties can be encoded in a unifying framework of a skew-symmetric convective term. This is made visible when the primitive variables (ρ, $\rho\mathbf{u}$, ρe) are transferred into so-called *square-root variables* (it is assumed that all quantities have been non-dimensionalized):

$$\mathbf{h} = (\sqrt{\rho},\ \sqrt{\rho}\,\mathbf{u}/\sqrt{2},\ \sqrt{\rho e})^T. \tag{3}$$

The L_2-norm of the square-root state vector $\mathbf{h}$ is equal to the sum of the mass and total energy in a periodic domain V:

$$||\mathbf{h}||_V^2 = \int_V \left(\rho + \tfrac{1}{2}\rho\,\mathbf{u}\cdot\mathbf{u} + \rho e\right)\,\mathrm{d}\mathbf{x} = \int_V \rho\,\mathrm{d}\mathbf{x} + \int_V \rho E\,\mathrm{d}\mathbf{x}. \tag{4}$$

The evolution equations (1) for the mass and total energy density feature only terms in divergence or gradient form, and therefore these quantities are conserved on the periodic domain V. Thus, analytically, the norm $||\mathbf{h}||_V$ is constant and bounded. For *in*compressible flow this is enough to develop unconditionally stable finite-volume semi-discretizations [22–24]. For compressible flow the situation is more subtle. Theoretically, we have not yet been able to prove the boundedness of the individual flow variables ($\mathbf{u}$, e) contributing to (4). In practice, however, a discretization that discretely preserves the bound on $||\mathbf{h}||_V$ is found to result in good stability properties for subsonic compressible flow, as we will show below.

The conservation properties of the Navier–Stokes equations are reflected in the skew-symmetry of the convective term when written in square-root variables (3). Let ϕ denote one of these variables, then elementary analysis shows that the convective part of its evolution reads

$$\partial_t\phi + \mathcal{C}(\mathbf{u})\phi,\ \text{with}\ \mathcal{C}(\mathbf{u})\phi \equiv \tfrac{1}{2}\nabla\cdot(\mathbf{u}\phi) + \tfrac{1}{2}\mathbf{u}\cdot\nabla\phi. \tag{5}$$

Inspection learns that the adjoint of the convective operator $\mathcal{C}(\mathbf{u})$ is equal to $-\mathcal{C}(\mathbf{u})$. In other words, the convective operator $\mathcal{C}(\mathbf{u})$ in (5) is skew-symmetric, $\mathcal{C}^T = -\mathcal{C}$, which we want to hold too in a discrete setting.

Next, it is noted that all quantities of interest (mass, momentum, ...) can be written as a product of two of the square-root variables:

$$\rho = (\sqrt{\rho})(\sqrt{\rho});\quad \rho\mathbf{u} = (\sqrt{\rho})(\sqrt{\rho}\mathbf{u});\quad \rho\mathbf{u}^2 = (\sqrt{\rho}\mathbf{u})(\sqrt{\rho}\mathbf{u});\quad \rho e = (\sqrt{\rho e})(\sqrt{\rho e}). \tag{6}$$

Therefore, consider the evolution of products of two square-root variables, say ϕ and ψ. If their convective transport is given by Eq. (5), and non-convective terms are ignored, then the evolution of the product $\phi\psi$ is given by

$$\partial_t(\phi\psi) = -\psi\mathcal{C}(\mathbf{u})\phi - \phi\mathcal{C}(\mathbf{u})\psi = -\nabla\cdot(\mathbf{u}\phi\psi). \tag{7}$$

Because the right-hand side in (7) is a divergence form, on a periodic domain the integral norm of the product vanishes. This demonstrates that all interesting quantities (6) are conserved by convective transport due to the skew symmetry of the square-root formulation $\mathcal{C}(\mathbf{u})$.

It is elegant that multiple conservation properties can be encoded in one mathematical symmetry property, which makes it relatively easy to develop a discretization method with similar (primary and secondary) properties. Moreover, it additionally allows for more properties, as discussed above, which may be relevant depending upon the application pursued. The next section gives some technical details.

3.2. Discretization on a curvilinear grid

A spatial discretization on a curvilinear grid is derived most easily in computational space ξ rather than physical space $\mathbf{x}$. Integration of physical quantities requires multiplication of (5) with the determinant $\mathcal{J}$ of the Jacobian matrix $J \equiv \frac{\partial \mathbf{x}}{\partial \xi}$ [60,61]. By setting $\mathbf{A}^{\xi_j} \equiv \mathcal{J} \frac{\partial \xi_j}{\partial x_i}$, which can be viewed as the area vector in the j-direction in computational space, and using $\frac{\partial}{\partial \xi_j}\left(\mathbf{A}^{\xi_j}\right) = 0$ [9, Appendix A], the convective part of the flow equations can be written as (Einstein convention)

$$\mathcal{J}\partial_t \phi + \tfrac{1}{2}\frac{\partial}{\partial \xi_j}\left(\mathbf{A}^{\xi_j}\cdot\mathbf{u}\phi\right) + \tfrac{1}{2}(\mathbf{A}^{\xi_j}\cdot\mathbf{u})\frac{\partial \phi}{\partial \xi_j} = \dots . \tag{8}$$

This form expresses the analytic skew-symmetry in computational space, cf. (5), and we want this property to hold in a discrete setting too.

In first instance, its discrete form is only skew-symmetric if the area vectors $\mathbf{A}^{\xi_j}$ are discretized at cell centers. Because the discretization should be implemented in a finite-volume method, the area vectors should be located at cell faces of a grid cell. Thus some consistent form of interpolation between cell centers and cell faces is required, to be discussed next.

After multiplication by $\Delta\xi^3$, the second term in Eq. (8) can be discretized at the cell center $k = (i, j, k)$ by substitution of a central second-order finite-volume discretization in computational space in terms of face variables as

$$\tfrac{1}{2}\sum_{f\in F_k}(\mathbf{A}_f\cdot\mathbf{u}_f)\tfrac{1}{2}\left(\phi_k + \phi_{\mathrm{nb}(f)}\right) . \tag{9}$$

Here, F_k is the set of faces of the grid cell with index k, whereas $\mathrm{nb}(f)$ is the neighbor of cell k which shares the face f. Further, $\mathbf{u}_f$ is some second-order accurate interpolation of the velocity vector to the faces and $\mathbf{A}_f$ is the face area vector pointing out of the cell. There is still freedom to choose these quantities, which we will exploit below when comparing with existing finite-volume methods.

The third term of the skew-symmetric form in Eq. (8) can be discretized by second-order discretization at the cell face f of the cell k normal to the direction ξ_j in computational space

$$\left(\Delta\xi^2\mathbf{A}^{\xi_j}\right)\cdot\mathbf{u}\Delta\xi\frac{\partial\phi}{\partial\xi_j} \approx (\mathbf{A}_f\cdot\mathbf{u}_f)\left(\phi_{\mathrm{nb}(f)} - \phi_k\right) ,$$

after which interpolation of these cell-face discretizations to the cell center gives

$$\tfrac{1}{2}\sum_{f\in F_k}\tfrac{1}{2}(\mathbf{A}_f\cdot\mathbf{u}_f)\left(\phi_{\mathrm{nb}(f)} - \phi_k\right) . \tag{10}$$

Summation of the two proposed spatial discretizations (9) and (10) gives

$$\Omega_k\partial_t\phi_k + \sum_{f\in F_k}\tfrac{1}{2}(\mathbf{A}_f\cdot\mathbf{u}_f)\phi_{\mathrm{nb}(f)} = \dots , \tag{11}$$

with Ω_k the cell volume. Observe how the terms with the central ϕ_k cancel, and how the coefficient of neighbor $\phi_{\mathrm{nb}(f)}$ only depends on face values. In this respect, note the importance of the interpolation factors $\frac{1}{2}$, irrespective of the geometry of the grid cells. Hence, starting from a skew-symmetric analytic operator, we created a skew-symmetric discrete operator. As shown in Sect. 3.1, it conserves discrete products of the basic square-root variables (3). This then leads to the desired discrete primary and secondary conservation properties.

3.3. Relation to finite-volume methods

The relation with existing finite-volume methods can be shown by constructing the discrete counterpart of Eq. (7). If the evolution of discrete square-root variables is governed by Eq. (11) and exact time-integration is assumed, then some analysis shows that products of discrete square-root variables satisfy

$$\Omega_k\partial_t(\phi_k\psi_k) + \sum_{f\in F_k}(\mathbf{A}_f\cdot\mathbf{u}_f)\tfrac{1}{2}\left(\phi_k\psi_{\mathrm{nb}(f)} + \phi_{\mathrm{nb}(f)}\psi_k\right) = \dots ,$$

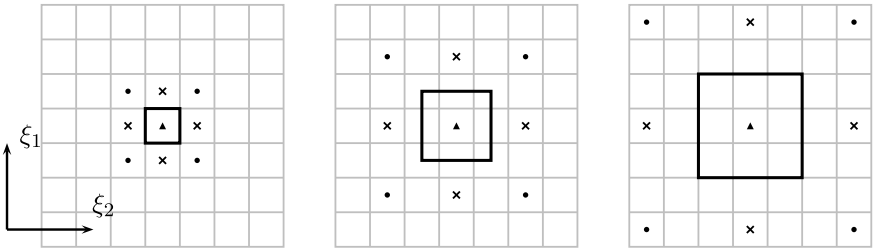

Fig. 2. The control volumes and stencils of the Δ, 2Δ, and 3Δ control volumes used for Richardson extrapolation of the convective and diffusive terms in collocated computational space.

where the dots denote non-convective terms. The expression $\left(\phi_k\psi_{\mathrm{nb}(f)} + \phi_{\mathrm{nb}(f)}\psi_k\right)/2$ is a local flux function as it is symmetric. Therefore, this is a finite-volume discretization of the convective terms for all possible products of square-root variables. As examples, the corresponding finite-volume discretizations of the mass and momentum equations read

$$\text{mass:} \qquad \Omega_k \partial_t \rho_k + \sum_{f\in F_k} (\mathbf{A}_f \cdot \mathbf{u}_f)\sqrt{\rho}_k \sqrt{\rho}_{\mathrm{nb}(f)} = \dots, \tag{12}$$

$$\text{momentum:} \qquad \Omega_k \partial_t (\rho\mathbf{u})_k + \sum_{f\in F_k} (\mathbf{A}_f \cdot \mathbf{u}_f)\sqrt{\rho}_k \sqrt{\rho}_{\mathrm{nb}(f)} \tfrac{1}{2}\left(\mathbf{u}_{\mathrm{nb}(f)} + \mathbf{u}_k\right) = \dots. \tag{13}$$

The energy equation is similar, and can be found in [52,9].

Outside the diagonal, the proposed discretization in (13) is skew-symmetric for any interpolation of the face velocity $\mathbf{u}_f$ and face area $\mathbf{A}_f$. On the diagonal, the coefficient of $\mathbf{u}_k$ in (13) equals half the discrete divergence from (12). This is in accordance with the analytical property that the operator $\phi \mapsto \nabla\cdot(\mathbf{m}\phi) - \frac{1}{2}(\nabla\cdot\mathbf{m})\phi$ is skew-symmetric for any mass flux $\mathbf{m}$, which corresponds with discrete energy conservation [42,62].

The discretization is second-order accurate if the interpolations $\mathbf{u}_f$ and $\mathbf{A}_f$ to the cell faces and the discretization of Ω_k at cell centers are second-order accurate in computational space. Some possible second-order accurate interpolations of the velocity vector $\mathbf{u}$ to the cell faces are

$$\mathbf{u}_f = \tfrac{1}{2}\frac{\rho_k + \rho_{\mathrm{nb}(f)}}{\sqrt{\rho}_k\sqrt{\rho}_{\mathrm{nb}(f)}}\tfrac{1}{2}\left(\mathbf{u}_k + \mathbf{u}_{\mathrm{nb}(f)}\right), \tag{14}$$

$$\mathbf{u}_f = \frac{1}{\sqrt{\rho}_k\sqrt{\rho}_{\mathrm{nb}(f)}}\tfrac{1}{2}\left(\rho_k\mathbf{u}_k + \rho_{\mathrm{nb}(f)}\mathbf{u}_{\mathrm{nb}(f)}\right), \tag{15}$$

and

$$\mathbf{u}_f = \tfrac{1}{2}\left(\mathbf{u}_k + \mathbf{u}_{\mathrm{nb}(f)}\right). \tag{16}$$

It can be shown [52] that the first interpolation (14) is equivalent to the finite-volume discretizations proposed by Jameson [38], Subbareddy and Candler [45], and Morinishi [40]. The second interpolation (15) results in the finite-volume discretization proposed by Kok [8], whereas the third interpolation (16) is used in simulations with symmetry-preserving regularization models [41,50,51,54].

In the accurate numerical simulations presented in this paper, the first interpolation (14) has been used. A comparison with the other two interpolations can be found in [52]. Also, details about the (standard) implementation of the pressure terms, the viscous terms and the heat diffusion can be found there.

3.4. Higher-order accurate discretizations

Fourth-order accurate versions of the above discretizations can be obtained by means of Richardson extrapolation, combining different stencils while preserving all conservation properties:

$$\alpha_1 R_k^{\Delta} + \alpha_2 R_k^{2\Delta} + \alpha_3 R_k^{3\Delta}, \tag{17}$$

where R symbolizes a discrete stencil with the subscript denoting its width (see Fig. 2).

By setting the leading terms in the Taylor expansion corresponding with (17) equal to zero, a one-parameter family of discretizations is obtained [8]:

$$\alpha_1 = (9-5\gamma)/8,\ \alpha_2 = \gamma,\ \alpha_3 = -(1+3\gamma)/8. \tag{18}$$

For a first derivative, the error in wave number space is small if the free parameter is set to $\gamma = -0.6668$ [8]. For this parameter value, in computational space the derivative is equivalent to the dispersion-relation-preserving (DRP) discretization proposed by Tam and Webb [63].

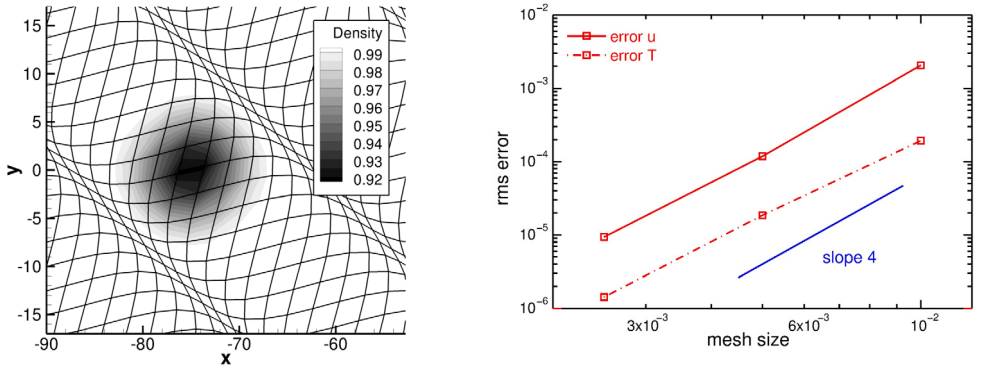

(a) Highly-irregular grid

(b) Error in velocity and temperature

Fig. 3. Grid refinement on a purposely highly-irregular grid around a convected vortex at $t = 125$. Ensolv is used with a fourth-order accurate discretization in computational space.

3.5. Grid refinement study for a two-dimensional vortex

To demonstrate grid-convergence of the proposed discretization method, we first present a study of a flow problem on a highly irregular grid. The accuracy of the above discretization is assessed using a fourth-order simulation of a two-dimensional vortex at Mach number $M = 0.5$ and Reynolds number $Re = 5$. In the inviscid limit, the vortex is convected with the mean flow isentropically, and the problem has an analytical solution [8]. The computational domain is two-dimensional: $[-100, 100]^2$. The grid is highly stretched on purpose in order to assess the performance of the skew-symmetric discretization on stretched curvilinear grids. Simulations are performed from time $t = 0$ to $t = 150$, in which the vortex travels 150 length scales. Three grids have been used: coarse 100×100 grid, medium 200×200 grid and fine 400×400. Fig. 3(a) shows the coarse computational grid in a small region around the vortex.

In the inviscid limit, the available analytical solution can be used to assess the accuracy of the method. For the viscous case, the right-hand side of the compressible Navier–Stokes equations is chosen such that this analytical solution is the exact solution of the problem (method of manufactured solutions, e.g. [64]).

A global numerical error is defined as the root-mean-square of the error of the numerical solution compared with the exact solution in computational space. Fig. 3(b) shows the errors in the horizontal velocity and the temperature, respectively, as a function of the mesh spacing in computational space. The global solution displays fourth-order accurate behavior, also for a curvilinear grid with considerable (but smooth) stretching. Thus, a skew-symmetric discretization forms a good basis for accurate simulations of compressible, turbulent flow past a delta wing to be described next.

4. The delta wing and its aerodynamics

To assess the applicability of the developed simulation method to large-scale simulation of practical turbulent flows, simulations of the subsonic transitional flow over a simple delta wing have been performed. This delta wing has been studied experimentally by Riley and Lowson [56]. An impression of the flow is shown in Fig. 1 above. Here we give some more information about this flow to guide the validation that will be presented in Sect. 6.

The focus of this study is on the transition to turbulence of the flow above the delta wing. Therefore, the chord Reynolds number, Mach number, and angle of attack have been selected to exclude other aerodynamic phenomena. The vortical flow structures do not break down above the wing, because the angle of attack is relatively small [65,66]; also, shock waves are absent.

The flow over the delta wing is dominated by a system of conical vortices above the delta wing [56,67], formed by the shear layer that separates at the leading edge of the delta wing. Under the influence of pressure differences, this shear layer rolls up into two large conical counter-rotating primary vortices (Fig. 1). They reduce the pressure along the upper surface of the wing and herewith increase the aerodynamic performance. Furthermore, the primary vortices induce an outboard flow over the upper surface of the delta wing. As a result, the boundary layer on the surface separates forming a secondary vortex, which counter-rotates with respect to the primary vortex.

Fig. 4 shows a global tubular structure of vortex pairs, as visualized by the Q-criterion (the second invariant of the velocity gradient). Each pair consists of a thin sub-structure with a high vorticity and a sub-structure with low vorticity. It seems that the sub-structures with low vorticity are wrapped around the sub-structures with high vorticity.

4.1. Break-up into sub-vortices

Fig. 1 shows more detailed axial slices of the instantaneous vorticity magnitude obtained in simulations on a fine grid. For $Re_c = 150,000$, the separated shear layer becomes unsteady at approximately $x = 0.6c$ and has broken into discrete

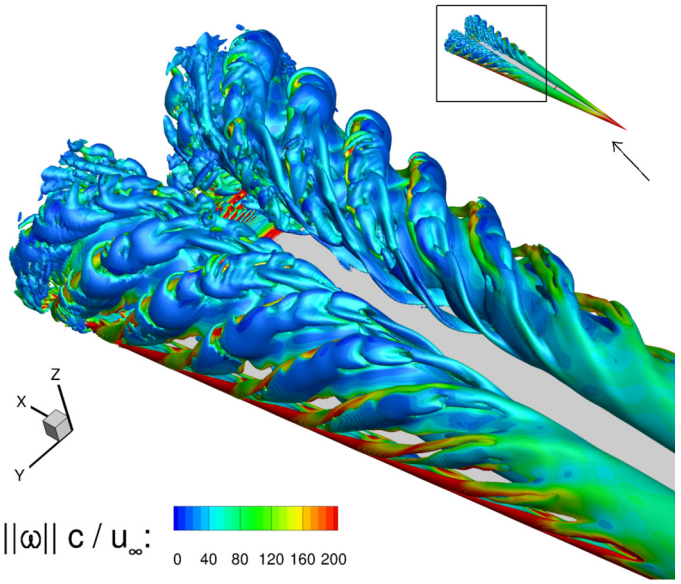

Fig. 4. An impression of the vortical structures over the delta wing, visualized by the zero iso-surface of the Q-criterion and colored by the vorticity magnitude.

sub-vortices at $x = 0.8c$. The sub-vortices deform as they travel along the shear layer, and near the trailing edge the deformations have caused so many irregularities in the flow that identification of the discrete sub-vortices becomes challenging, i.e. the flow has become turbulent.

Although discrete vortical sub-structures have been first observed in 1985 [68], there is no consensus on the physics of this phenomenon. On the one hand, in physical and numerical experiments by Gad-el Hak and Blackwelder [68] and Visbal and Gordnier [69,70] only *unsteady* sub-vortices have been observed, which counter-rotate with respect to the time-averaged direction of the flow. On the other hand, in experiments by Payne et al. [71] and Washburn and Visser [72] only *steady* discrete sub-vortices are encountered, which co-rotate around the primary vortex in the same direction as the flow. Reynolds and Abtahi [73] as well as Riley and Lowson [56] experimentally observe *both* steady co-rotating and unsteady counter-rotating sub-vortices.

The relation between the unsteady and steady sub-vortices is not clear. In their LDV experiments, Riley and Lowson [56] observe that, under some conditions, the steady co-rotating sub-vortices seem to be distorted by the unsteady counter-rotating sub-vortices. The latter are observed to be easily triggered by physical or numerical perturbations [56,74], and have a long perseverance. In fact, Reynolds and Abathi [73, p. 3] observe that they "decay approximately one-half hour after the last disturbance", thus overwhelming the steady co-rotating sub-vortices.

4.2. Data of the Riley and Lowson experiments

Next, the setup and the results of the LDV experiments by Riley and Lowson [56] are summarized. The delta wing used has a blunt trailing edge, a root chord length of $c = 471\,\text{mm}$ and a thickness of $t = 11.5\,\text{mm}$. The sweep angle is $\Lambda = 85°$, which makes the delta wing very slender. The bevel angle is 30° and the angle of attack $\alpha = 12.5°$. The experiments were conducted for a range of Reynolds numbers $\text{Re}_c \equiv \rho_\infty u_\infty c/\mu_\infty$, with c the chord length. The non-dimensional distance from the leading edge is given by the local Reynolds number $\text{Re}_x \equiv \text{Re}_c(x/c)$. The simulations will be performed at $\text{Re}_c = 150,000$ and $211,200$. The free-stream Mach number is $\text{M} = 0.3$.

In the experiments for Re_c smaller than $160,000$, Riley and Lowson [56, Fig. 8] observe a Kelvin-Helmholtz-type instability which originates around $\text{Re}_x \approx 78,000$ and evolves into transitional flow around $\text{Re}_x = 129,000$. At higher chord Reynolds numbers, e.g. $\text{Re}_c = 211,200$, no Kelvin-Helmholtz waves are observed, but instead steady structures. The flow becomes transitional around $\text{Re}_x \approx 129,000$ and appears fully turbulent around $\text{Re}_x \approx 200,000$.

5. Numerical simulation and verification

In this section, results of the accurate numerical simulations are presented. Firstly, the spatial discretization is re-iterated, followed by a description of the used computational grids. Thereafter, the time-integration method is summarized. Finally, the parallel implementation is described. The numerical verification (grid refinement and convergence of the flow statistics) finalizes this section. The validation with experimental data will be given in Sect. 6.

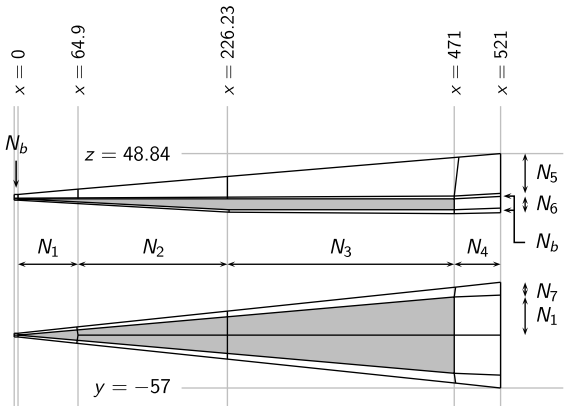

Fig. 5. A side view (top) and top view (bottom) of the grid blocks around the delta wing and the dimensions of the grid. The locations are given in mm.

Table 1
The dimensions of the block above the delta wing for the coarse, medium, and fine grid (see Fig. 5).

	N_b	N_1	N_2	N_3	N_4	N_5	N_6	N_7
coarse	8	56	504	304	40	48	32	16
medium	11	78	693	418	44	66	44	22
fine	16	112	1008	608	80	96	64	32

5.1. Numerical model

Space discretization. The simulations have been performed with the proposed symmetry-preserving finite-volume discretization. For the convective terms and the pressure gradient, the dispersion-relation-preserving fourth-order accurate discretization has been used [8]. The viscous terms have been discretized using a standard fourth-order accurate discretization.

The use of artificial dissipation is not necessary for numerical stability, yet a low level of sixth-order artificial dissipation (with $k_6 = 1/8$) has been added [58]. The purpose of the low level of artificial dissipation is to smoothen unphysical oscillations in the numerical solution resulting from deficiencies of the smoothness of the grid, for example at the apex and the sharp edges of the wing.

At the boundaries of the computational domain, far-field boundary conditions based on Riemann invariants are applied. To prevent spurious reflections at outflow boundary conditions, and to dissipate sufficient kinetic energy in the under-resolved far field, the strength of the artificial dissipation is increased outside the region of interest.

Grid. A cubic computational domain with a length of 21 chord lengths has been used. The origin of the coordinate system is at the apex of the delta wing. The x-axis is aligned with the chord line of the wing, the z-axis is normal to the upper surface, and the y-axis is aligned with the span.

To capture the boundary layer, the wing is covered by thin boundary layer blocks, giving a fine grid near the surface of the wing; see Fig. 5. Above the wing, conical blocks are used to capture the primary vortex. These blocks grow linearly in the axial direction at approximately the same rate as the primary vortex. A wedge-shaped block is used at the apex of the wing, which prevents collapsing edges of the conical blocks at the apex. Details can be found in [52].

The transitional flow over the delta wing at $\mathrm{Re_c} = 150,000$ has been computed on a coarse, a medium, and a fine computational grid. The fine grid is obtained by refining the coarse grid by a factor two in each direction, and the medium grid is obtained by refining the coarse grid by a factor 1.5. At the chord Reynolds number $\mathrm{Re_c} = 211,200$, only a simulation on the medium grid has been performed. The dimensions of the three grids are given in Table 1 (see also Table 2). To study the reliability of the converged flow statistics, a grid refinement study is performed below. Fig. 6 shows a detail of the surface grid and a slice of the coarse grid at $x = 0.8c$.

The grids used are approximately isotropic throughout the primary vortex downstream from the end of the wedge block at $x = 64.9\,\mathrm{mm}$. The dimensions of the grid cells of the fine grid in the primary vortex increase approximately linearly from $\Delta x = 0.08\,\mathrm{mm}$, $\Delta y = 0.05\,\mathrm{mm}$, and $\Delta z = 0.10\,\mathrm{mm}$ at the end to the wedge block at the leading edge, to $\Delta x = 0.57\,\mathrm{mm}$, $\Delta y = 0.40\,\mathrm{mm}$, and $\Delta z = 0.44\,\mathrm{mm}$ at the trailing edge.

Time integration. Time integration is performed using a four-stage low-storage explicit Runge-Kutta method with a small time step size. The initial condition of the simulations is obtained by performing a RaNS simulation with a k-ω model. No perturbations are added to the initial condition.

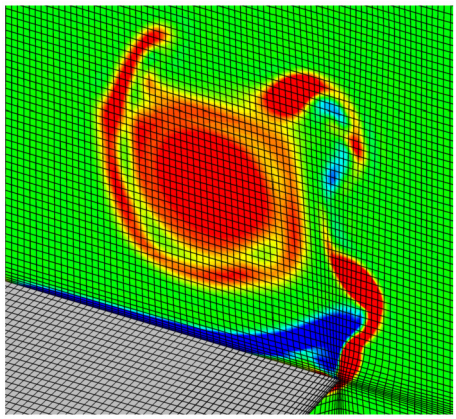

Fig. 6. The coarse mesh on the wing surface and at the axial slice $x = 0.8c$. Note that the grid is approximately isotropic in the primary vortex.

Table 2
The number of blocks used in simulations of the delta wing, and the average wall clock time of a time step T_{step}, showing good weak scalability.

	N_{cells}	N_{blocks}	N_{cores}	T_{step} (s)
coarse	1.96×10^7	6324	192	0.90
medium	4.36×10^7	6073	480	0.83
fine	1.33×10^8	6744	1920	0.79

The time step size normalized by the free-stream flow velocity and the chord length of the wing is $\Delta t u_\infty / c = 8.0 \times 10^{-6}$ on the coarse grid, 4.5×10^{-6} on the medium grid, and 2.2×10^{-6} on the fine grid. The simulations at $\text{Re}_c = 150,000$ on the coarse and medium grid are performed from time $t u_\infty / c = 0$ to $t u_\infty / c = 20$, which corresponds to 20 convective time units. The simulation on the fine grid is performed for 17 convective time units. The simulation at $\text{Re}_c = 211,200$ on the medium grid is performed for 13 convective time units. After 2 convective time units the flow has transitioned to turbulence, and the collection of flow statistics starts. In Sect. 5.3 it will be verified that this procedure is sufficiently accurate.

Parallelization and CPU performance. The simulations have been performed on the Dutch national supercomputer Cartesius. Ensolv has been parallelized using a hybrid OpenMP/MPI implementation. The computational grids are divided into a large number of small blocks that are distributed over domains using a graph-based domain decomposition. Each MPI process computes the flow in the blocks of an assigned domain. Within a domain, OpenMP parallelization is applied on the blocks. The number of blocks and the parallel performance of the simulations is listed in Table 2, showing good weak scalability. As a result, the longer simulations with around 5 million time steps take 1-2 months wall-clock time in the indicated configuration.

5.2. Grid refinement

The numerical quality of the solution is assessed first by studying the convergence upon grid refinement for $\text{Re}_c = 150,000$ on the three grids: coarse, medium and fine. Results for several quantities will be presented: turbulent kinetic energy, velocity, pressure and vorticity.

Turbulent kinetic energy. Fig. 7 shows the turbulent kinetic energy on lines through the separated shear layer obtained on different grids. Although turbulent kinetic energy is relatively sensitive to the grid resolution compared to the time average of the velocity and pressure (see below), the turbulent kinetic energy obtained on the medium and fine grids show good agreement. The shear layer becomes unsteady at approximately the same axial location for the medium and the fine grid; the transition to unsteady flow seems to be delayed on the coarse grid. This suggests that (not surprisingly) the coarse grid is not fine enough to capture the transition to unsteady flow of the shear layer.

Time-averaged velocity. Fig. 8 shows the time-averaged axial velocity on a vertical line through the core of the primary vortex for the three grids. Note that the vertical axis has been split, with different scaling to enhance visibility of the velocity profile through the primary vortex. Fig. 9 shows the axial velocity on horizontal lines at different heights around the leading edge for the three grids. Both plots show convergence of the time-averaged velocity as the grid is refined. Although the agreement is not perfect, overall the time-averaged velocity obtained on the coarse grid agrees with the time average obtained on the medium and fine grid.

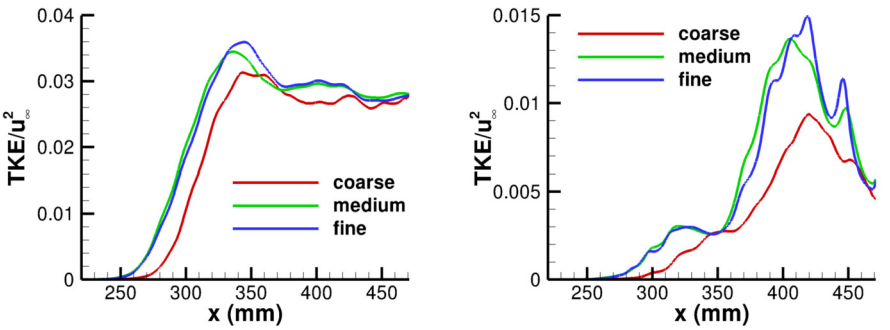

Fig. 7. The turbulent kinetic energy along a line above the leading edge at $z = 7.6\,\text{mm}$ (left) and along a line through the separated shear layer above the vortex core (right) at $\text{Re}_c = 150,000$.

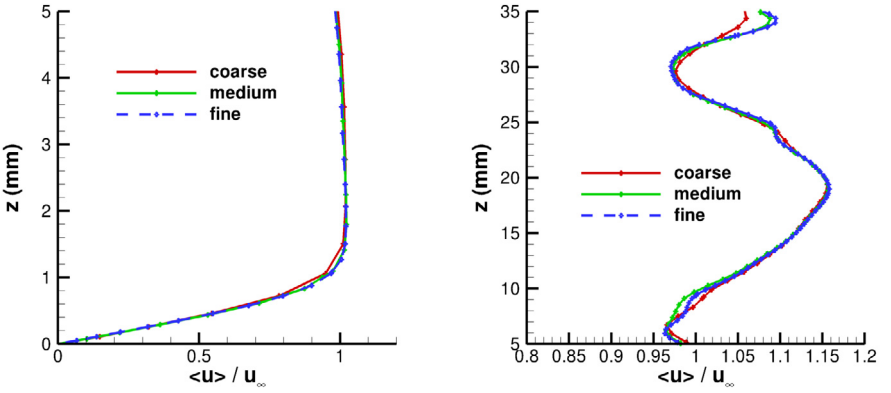

(a) Lower part. (b) Upper part.

Fig. 8. The time-averaged axial velocity at $\text{Re}_c = 150,000$ along a vertical line through the suction peak above the delta wing surface at $x = 0.9c$ and $y = 21.74\,\text{mm}$ at three different grid resolutions. The vertical axis has been split in two parts: the left-hand plot shows the velocity profile in the boundary layer. The right-hand plot (with different scaling) shows the velocity profile through the core of the primary vortex.

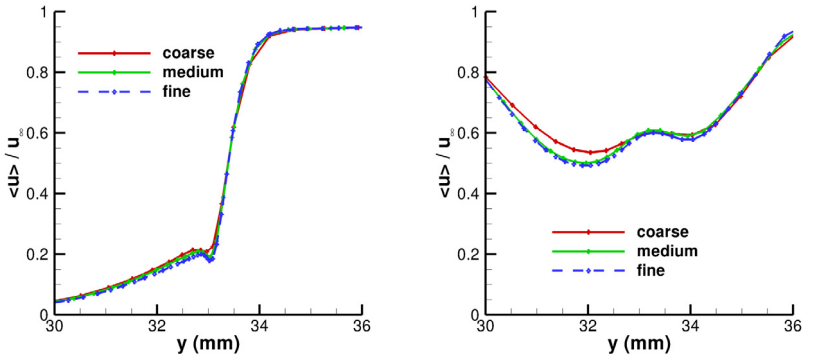

(a) Just above wing surface. (b) Higher above wing surface.

Fig. 9. The time-averaged axial velocity at $\text{Re}_c = 150,000$ along a horizontal line at $z = 0.1\,\text{mm}$ (left) and $z = 4.1\,\text{mm}$ (right) and at the axial location $x = 0.8c$ corresponding to $\text{Re}_x = 120,000$. At this axial location the leading edge of the wing is at $y = 32.97\,\text{mm}$.

Time-averaged pressure. Fig. 10 shows the time-averaged pressure coefficient on the upper surface of the delta wing and its behavior upon grid refinement. These time averages have converged in time, as shown in Sect. 5.3. The surface pressure seems to converge upon grid refinement for $x \leq 450\,\text{mm}$, i.e. away from the trailing edge. However, (slightly) different pressure coefficients are predicted for the coarse, medium, and fine grid at the trailing edge of the delta wing. Possibly, the grids do not have sufficient resolution to accurately capture the vortex shedding at the blunt trailing edge. Hence we are hesitating a bit to call our results a direct numerical simulation.

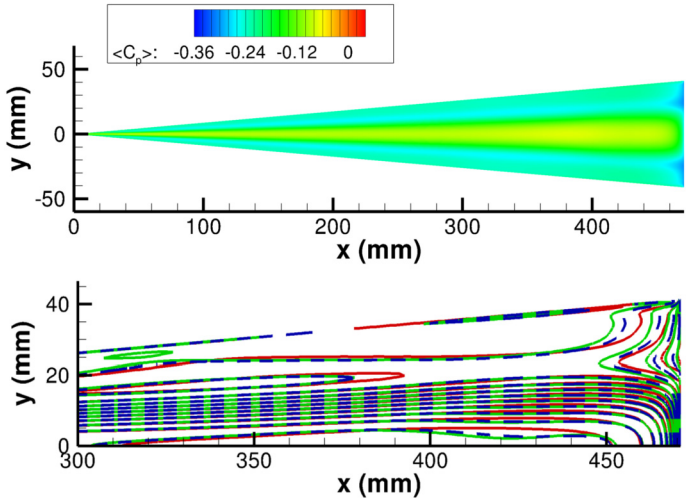

Fig. 10. The time-averaged pressure coefficient at the upper surface of the delta wing at $\mathrm{Re_c} = 150,000$. The top figure shows an overview obtained on the fine grid. The bottom figure shows a detailed (contour-plot) comparison with the results (blue) obtained on the coarse (red) and medium grid (green) in the trailing edge region (downstream of $x = 300\,\mathrm{mm}$). (For interpretation of the colors in the figure(s), the reader is referred to the web version of this article.)

Time-averaged vorticity. The top row in Fig. 11 shows the time average of the axial vorticity at $\mathrm{Re_c} = 150,000$, at three chord-wise locations. They correspond with, from left to right, local Reynolds numbers of $\mathrm{Re}_x = 100,000$, $\mathrm{Re}_x = 130,000$, and $\mathrm{Re}_x = 150,000$ (i.e. the trailing edge). The time-averaged shear layer is coherent for local Reynolds numbers up to $\mathrm{Re}_x = 90,000$ (not shown), but it breaks up at larger distances from the apex of the wing.

An impression of the influence of discretization error on this subtle physical behavior of the shear layer can be obtained by comparison with results on the medium and coarse grids, shown in the middle and bottom rows of Fig. 11. Their development on the medium grid agrees with results obtained on the fine grid, showing similar sub-structures, with only slight small-scale differences. However, on the coarse grid the time-averaged shear layer has not yet broken up at $\mathrm{Re}_x = 100,000$. Also, at higher local Reynolds numbers, the time-averaged sub-vortices obtained on the coarse grid are significantly weaker than the sub-vortices obtained on the medium and fine grids. This suggests that the instability process that causes break-up of the time-averaged shear layer is not captured accurately on the coarse grid. In the next section, these results will be validated with experimental measurements.

5.3. Convergence of flow statistics

In this paper, many results are presented for time-averaged quantities. Therefore, we first study the length of the averaging time interval needed to obtain reliable averages that may be interpreted with a physical eye. To study the sensitivity with respect to the averaging interval, flow statistics obtained with different sample intervals are compared.

Fig. 12 shows the time average of the axial vorticity at $x = 0.9c$ obtained with different averaging intervals at $\mathrm{Re_c} = 150,000$ on the fine grid (left) and at $\mathrm{Re_c} = 211,000$ on the medium grid (right). The contour lines have been chosen to highlight sub-structures, because these are of interest in the study of the shear layer. At the lower chord Reynolds number $\mathrm{Re_c} = 150,000$, the averaging intervals were 3 (red), 9 (green) and 18 (blue) periods; at the higher $\mathrm{Re_c}$ they were 3 (red), 7 (green) and 11 (blue). The time average of the axial vorticity is more sensitive to the used interval than the time average of the velocity. Yet, the time averages obtained over the two longer time intervals agree quite well, with the most variation in the results for $\mathrm{Re_c} = 211,000$. The latter is to be expected, as turbulent details will be smaller at higher Reynolds numbers; also a finer grid is likely to be required to accurately capture the flow structure. The plots suggest that many sub-structures can be observed in the mean axial vorticity, and they provide confidence in the interpretation of the vorticity plots presented in this paper.

6. Validation

In this validation section, the development of the separated shear layer is studied using the results of the simulations at the chord Reynolds numbers $\mathrm{Re_c} = 150,000$ on the fine and medium grid and the simulation at $\mathrm{Re_c} = 211,200$ on the medium grid. The results of the simulations are compared with the experiments by Riley and Lowson [56]. First, instantaneous flow phenomena are compared, thereafter we study time-averaged behavior.

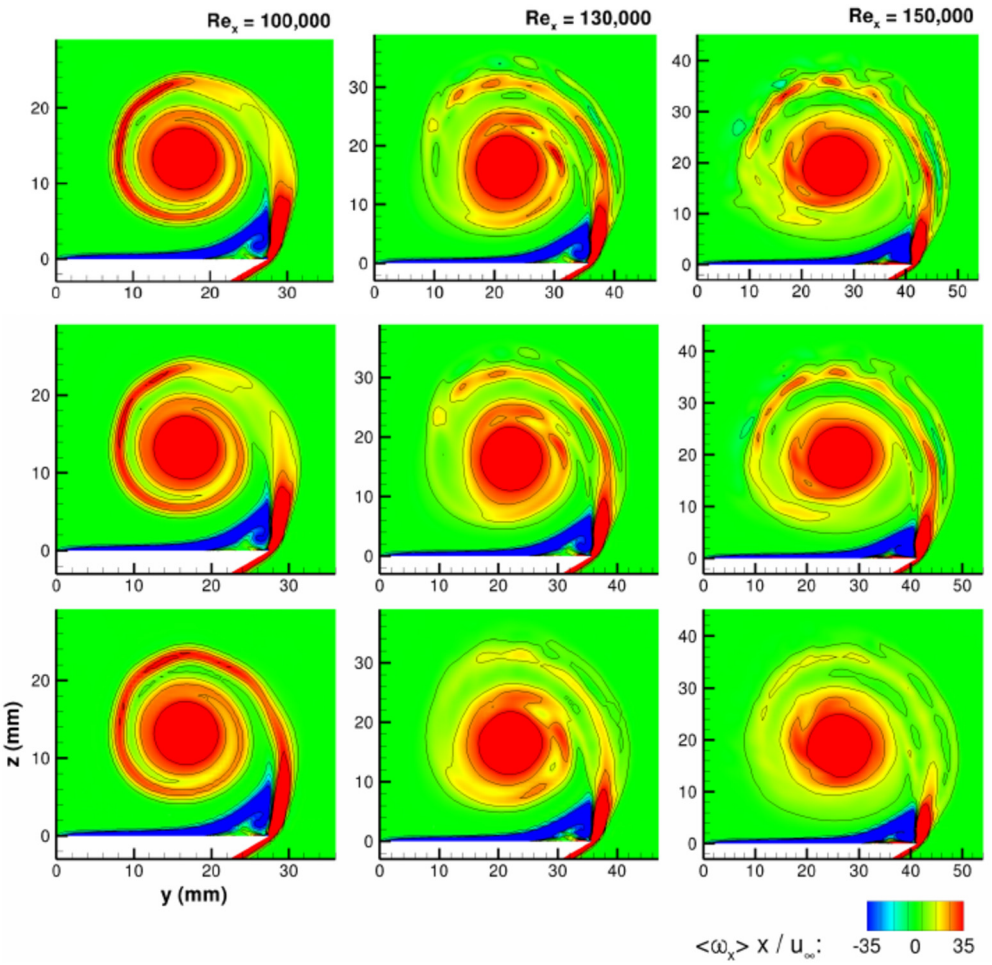

Fig. 11. Grid-refinement study for the axial slices of the scaled time-averaged axial vorticity at chord Reynolds number $\mathrm{Re_c} = 150,000$. From left to right, results are shown at three axial locations ($\mathrm{Re}_x = 100,000 - 150,000$) as obtained on the fine (top), medium (middle) and coarse (bottom) grids, respectively.

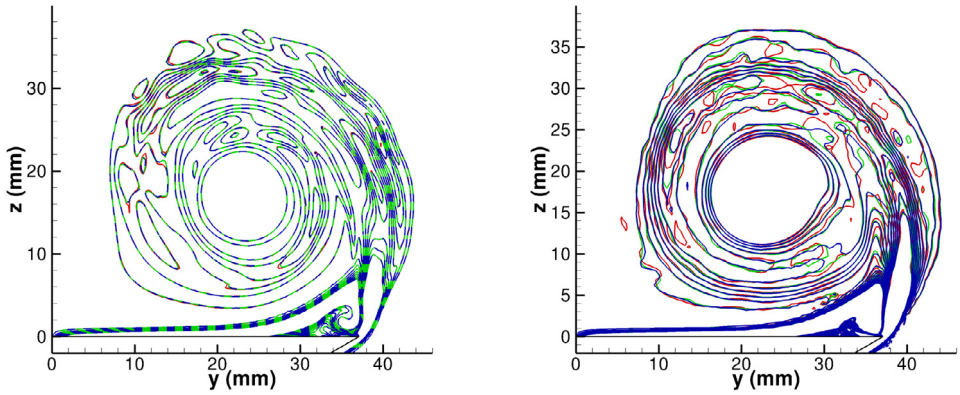

(a) $\mathrm{Re_c} = 150,000$: fine grid. (b) $\mathrm{Re_c} = 211,000$: medium grid.

Fig. 12. Axial slice at $x = 0.9c$ ($\mathrm{Re}_x = 135,000$) with contour lines of the mean axial vorticity $\langle\omega_x\rangle c/u_\infty$ at chord Reynolds number $\mathrm{Re_c} = 150,000$ on the fine grid (left) and $\mathrm{Re_c} = 211,000$ on the medium grid (right). Results for various averaging intervals have been plotted, as indicated by the color: red=short, green=medium and blue=long.

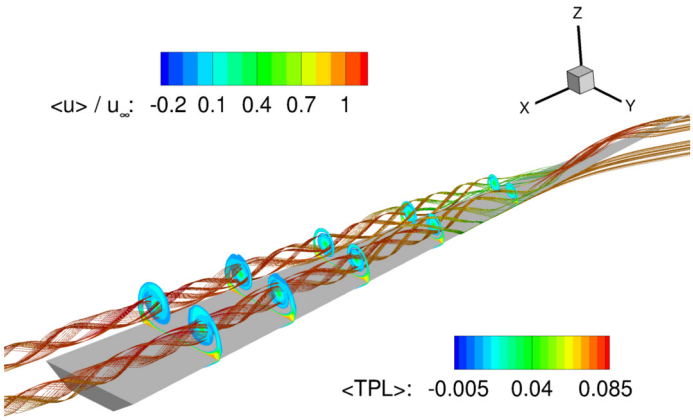

Fig. 13. Slices showing the time average of the total pressure loss and streamlines of the time-averaged velocity through the primary vortex colored by the mean axial velocity.

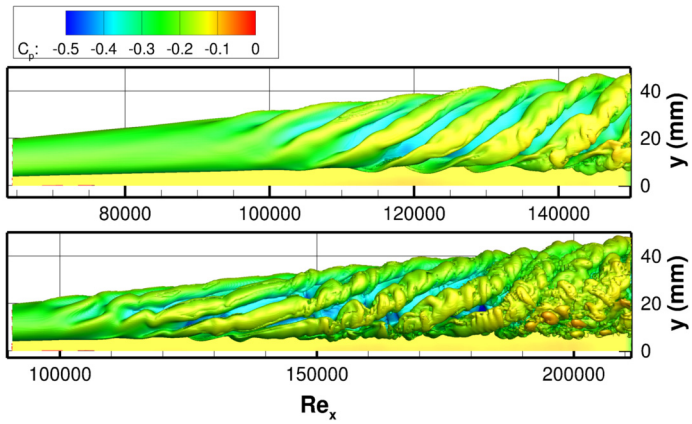

Fig. 14. Iso-surfaces of the vorticity magnitude $||\omega||c/u_\infty = 20$ colored by the pressure coefficient obtained on the medium grid at chord Reynolds numbers $\mathrm{Re_c} = 150,000$ (top) and $\mathrm{Re_c} = 211,200$ (bottom). The local Reynolds number Re_x correspond to the axial range $x = 200\,\mathrm{mm}$–$471\,\mathrm{mm}$.

6.1. Instantaneous flow phenomena

6.1.1. Sub-vortices

The instantaneous flow field over the delta wing is characterized by the break-up of the separated shear layer into sub-vortices and its transition to turbulence. Riley and Lowson [56, p. 50] attribute the onset of unsteady flow to a Kelvin-Helmholtz instability, that "went through a pairing mechanism similar to that in a simple two-dimensional shear layer"; see also [75].

The instantaneous sub-vortices above the delta wing lie in helical vortex tubes that counter-rotate. They wind around the primary vortex in the direction opposite to the mean flow velocity, as shown in the time-averaged simulation results visualized in Fig. 13. The vortex tubes are convected downstream with the flow velocity; they gradually deform and break up into smaller sub-vortices. This deformation process eventually causes transition of the separated shear layer.

Fig. 14 shows a top view of the sub-vortices obtained in simulations at the chord Reynolds numbers $\mathrm{Re_c} = 150,000$ and $\mathrm{Re_c} = 211,200$. Both plots correspond to the horizontal range $x = 200\,\mathrm{mm}$–$471\,\mathrm{mm}$, but the local Reynolds number $\mathrm{Re}_x = \mathrm{Re_c}(x/c)$ is used as the horizontal coordinate. The plots suggest that the evolution of the sub-vortices is related to the local Reynolds number Re_x, with for the eye visible vortices starting around $\mathrm{Re}_x \approx 95,000$ for both chord Reynolds numbers. The plot of the sub-vortices at $\mathrm{Re_c} = 211,200$ shows that the sub-vortices no longer form coherent helical structures downstream of $\mathrm{Re}_x \approx 200,000$ (axial location $x = 0.95c$). This is consistent with the observations of Riley and Lowson [56, Fig. 8], who call the flow fully turbulent there.

To study the role of the local Reynolds number in more detail, Fig. 15 shows axial slices of the axial vorticity obtained in the simulations at $\mathrm{Re_c} = 150,000$ (fine grid) and $\mathrm{Re_c} = 211,200$ (medium grid) for comparable local values of Re_x in the range $75,000 - 150,000$. Because of the symmetry (see Fig. 1), only results obtained at the starboard side of the wing are shown. By comparing both columns of plots in Fig. 15, the axial slices confirm that the development of the shear layer in the transitional range depends on the local Reynolds number. It is illustrative to compare the two bottom rows in Fig. 15 with a snapshot of the Riley and Lowson experiment in [56, Fig. 7] (at $\mathrm{Re}_x = 100,000$).

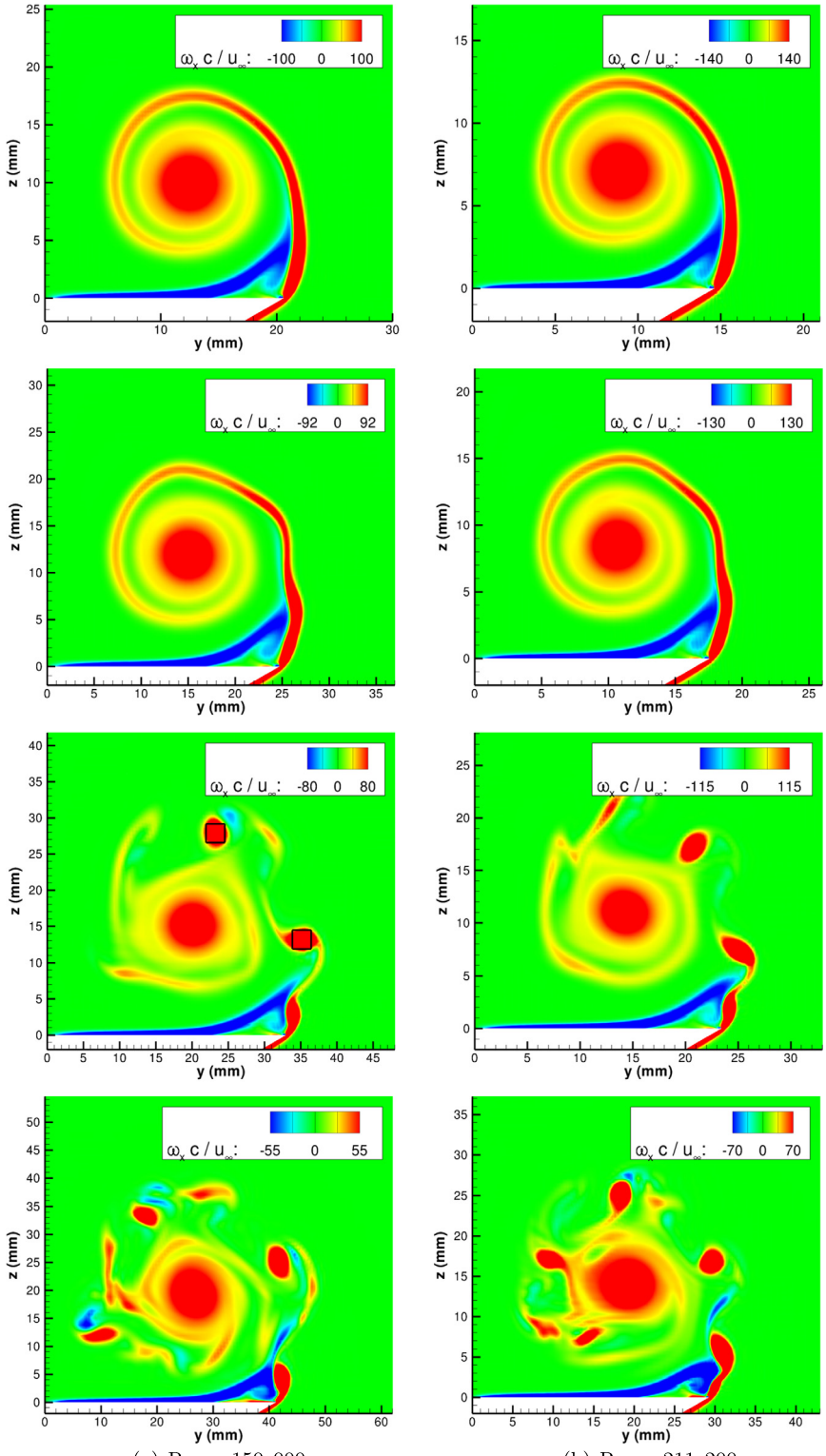

(a) $\mathrm{Re_c} = 150,000$ (b) $\mathrm{Re_c} = 211,200$

Fig. 15. Axial slices of the instantaneous axial vorticity at chord Reynolds numbers $\mathrm{Re_c} = 150,000$ (a) and $\mathrm{Re_c} = 211,200$ (b) at local Reynolds numbers $\mathrm{Re}_x = 75,000$, $\mathrm{Re}_x = 90,000$, $\mathrm{Re}_x = 120,000$, and $\mathrm{Re}_x = 150,000$ (top to bottom) obtained on the medium grid. For the latter three local Reynolds numbers, snapshots have been taken at times corresponding to approximately the same phase of the unsteady creation of discrete vortices.

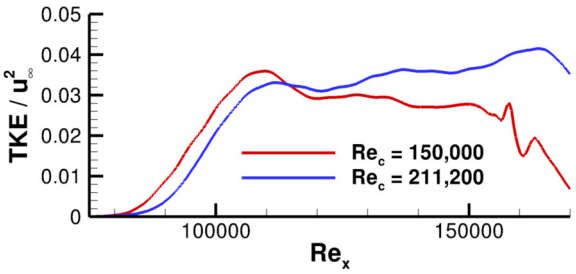

Fig. 16. The development of the turbulent kinetic energy on a line through the separated shear layer above the leading edge at $z = 7.6\,\text{mm}$ for $\text{Re}_c = 150,000$ and at $z = 5.3\,\text{mm}$ for $\text{Re}_c = 211,200$.

For both chord Reynolds numbers, the shear layer is steady and coherent at local Reynolds numbers up to $\text{Re}_x \approx 75,000$. The steady co-rotating sub-vortices, which have been observed in the experiments by Riley and Lowson [56] for chord Reynolds numbers larger than $\text{Re}_x \approx 30,000$, are not observed in the simulation. As mentioned in Sect. 4.1, experimental measurements suggest that steady co-rotating sub-vortices can be easily overwhelmed by the sensitive contra-rotating instabilities.

In the numerical simulations in the literature, steady sub-vortices seem only to be encountered on under-resolved grids. They have been observed in detached-eddy simulations at high-Reynolds number flow over a delta wing at the Netherlands Aerospace Center NLR for excessive levels of the artificial dissipation, but these are overwhelmed by unsteady counter-rotating sub-structures when the artificial dissipation is cut back [59]. Steady co-rotating sub-vortices have also been observed in detached-eddy simulations of high Reynolds number flow over a delta wing by Mitchell et al. [74], but upon grid refinement they disappear and counter-rotating unsteady sub-vortices appear. Yet, they have not been observed in simulations of an infinite triangular plate by Visbal and Gordnier [70]. The latter authors pay special attention to this apparent inconsistency in the observations.

6.1.2. Transition to turbulence

To determine the location of the onset of unsteady flow, Fig. 16 shows the turbulent kinetic energy as a function of the local Reynolds number on a line through the shear layer just above the leading edge. In the simulation at $\text{Re}_c = 150,000$ on the fine grid, the flow becomes unsteady at the axial location corresponding to a local Reynolds number of approximately $\text{Re}_x \approx 80,000$ (see also Fig. 7). This is similar to the instability at $\text{Re}_x \approx 78,000$ observed in the experiment [56]. In the simulation at $\text{Re}_c = 211,200$ on the medium grid, the flow becomes unsteady at approximately $\text{Re}_x \approx 85,000$, whereas it is postponed to approximately $\text{Re}_x \approx 129,000$ in the experiment.

While the transition location observed in the simulations at $\text{Re}_c = 150,000$ accurately agrees with the experiment, Riley and Lowson [56] observe a change in transition behavior at approximately $\text{Re}_c = 160,000$, which moves the onset of unsteady flow downstream. This change of the flow is not observed in the simulations. In fact, the results of the simulations suggest that the development of the simulated shear layer for the local Reynolds number $\text{Re}_c = 211,200$ is similar to the development at $\text{Re}_c = 150,000$. It seems that this difference can be attributed to the presence of unsteady sub-vortices in the simulation for $\text{Re}_c = 211,200$, whereas they are observed to disappear in the experiment (see the discussion in Sect. 4.1).

To further study the transition to full turbulence, Fig. 17 shows snapshots (obtained on the medium grid) of the instantaneous axial vorticity at $\text{Re}_c = 211,200$, which is closer near the trailing edge than shown in Fig. 15. At $x = 0.8c$ ($\text{Re}_x \approx 170,000$), coherent sub-vortices can still be distinguished. At the trailing edge $x = c$, the sub-vortices have gone through so many break-up processes that coherent sub-vortices are no longer visible. Thus, in simulations at $\text{Re}_c = 211,200$ the separated shear layer becomes turbulent near the trailing edge. This is in agreement with the experiment by Riley and Lowson [56] who observed 'full' turbulence around $\text{Re}_x \approx 200,000$.

In conclusion, the simulations confirm the gradual transition of the separated shear layer from coherent sub-vortices to turbulent flow observed in the experiments by Riley and Lowson [56]. In the simulations, the development of the shear layer is characterized by the local Reynolds number, as in [70]. The simulations do capture the unsteady sub-vortices, but not the steady sub-vortices observed in the experiments [56]. We come back to this issue in the next section on time-averaged results.

6.2. Time-averaged flow

In this section, the time averages of the flow over the delta wing are studied and compared with the LDV measurements by Riley and Lowson [56].

6.2.1. Time averages for $\text{Re}_c = 150,000$

For $\text{Re}_c = 150,000$, the time-averaged shear layer is coherent for local Reynolds numbers up to $\text{Re}_x \approx 90,000$, when the instantaneous flow field already has become unsteady. Fig. 18 shows a comparison of instantaneous versus time-averaged

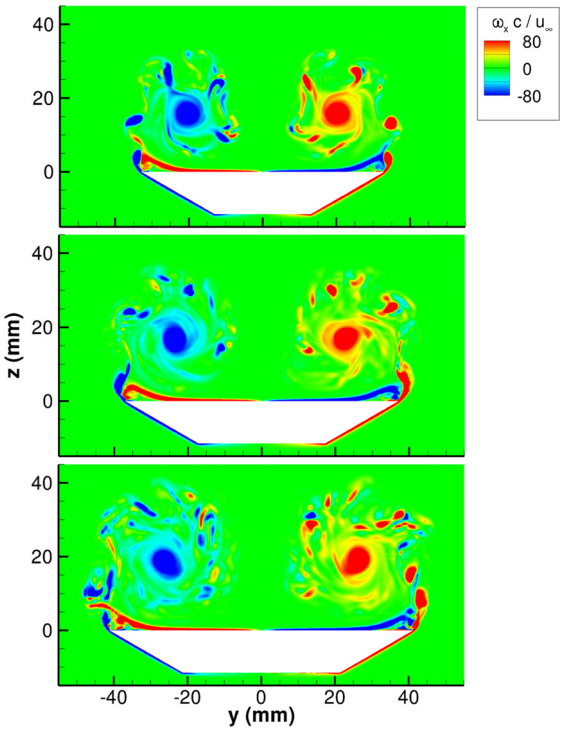

Fig. 17. Axial slices of the instantaneous axial vorticity at chord Reynolds number $Re_c = 211,200$ in the trailing edge region, at the axial locations $x = 0.8c$ ($Re_x \approx 170,000$) (top), $x = 0.9c$ ($Re_x \approx 190,00$) (middle), and $x = c$ (bottom). Note that the approximate symmetry of the sub-vortices is destroyed at approximately $x = 0.9c$.

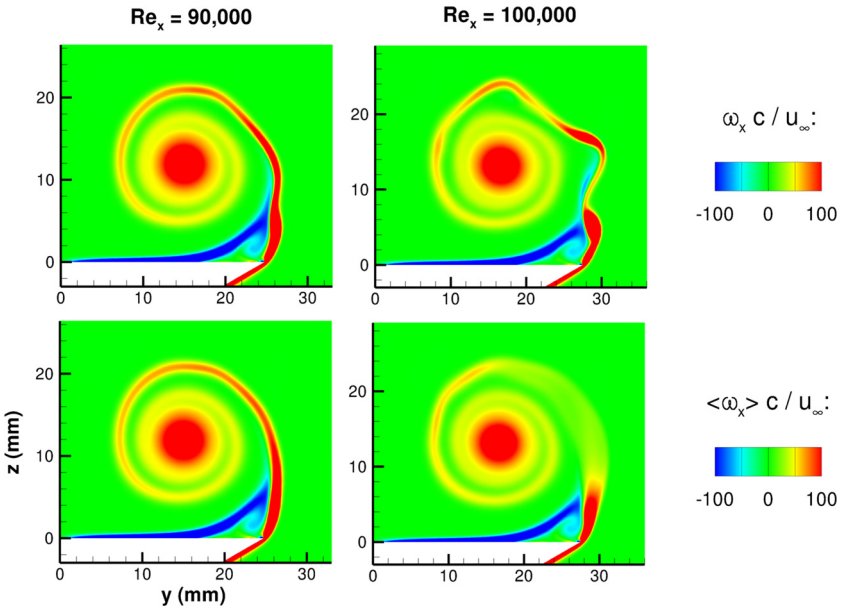

Fig. 18. Comparison of the instantaneous (top) and the time-averaged (bottom) axial vorticity before and after break-up of the separated shear layer in sub-vortices at $Re_c = 150,000$ computed on the fine grid.

axial vorticity. It can be seen that at $Re_x \approx 90,000$ the shear layer is unsteady but coherent, and the time-average shows a coherent shear layer. At $Re_x \approx 100,000$ the unsteady shear layer has broken up into discrete sub-vortices, and the time-averaged axial vorticity is reduced significantly in the region of the shear layer break-up. This suggests that the break-up of the time-averaged shear layer is directly related to the break-up of the unsteady shear layer.

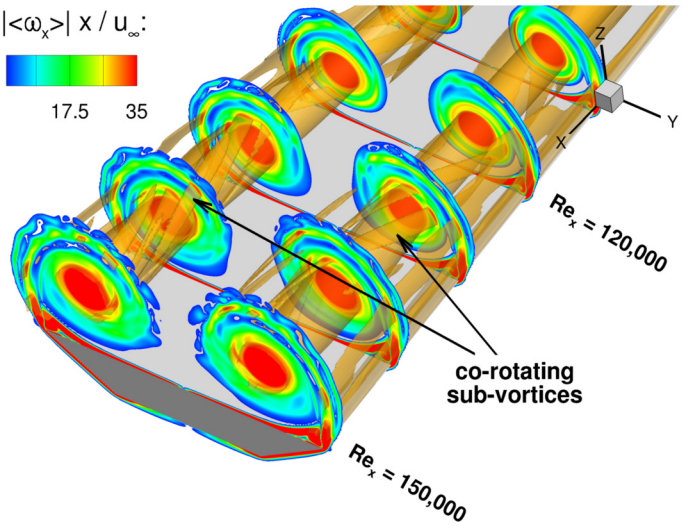

Fig. 19. Axial slices of the magnitude of the time-averaged axial vorticity scaled by the axial location $|\langle\omega_x\rangle|x/u_\infty$ at $\mathrm{Re_c} = 150,000$ computed on the fine computational grid. The iso-surface $|\langle\omega_x\rangle|x/u_\infty = 0.29$ shows that the time-averaged sub-vortices rotate around the vortex core in the same direction as the flow velocity.

To further study the spatial development of the time-averaged sub-vortices observed in the simulation, Fig. 19 shows a few axial slices of the time-averaged axial vorticity with an iso-surface corresponding to the sub-vortices. In the range $\mathrm{Re}_x \approx 120,000$–$150,000$ sub-structures can be observed in the time-averaged axial vorticity. This is approximately the same range of local Reynolds numbers as the steady sub-structures observed in the LDV measurements by Riley and Lowson [56]. The iso-surfaces show that the time-averaged sub-vortices lie in helical tubes that co-rotate with the flow, just as the steady sub-vortices observed by the latter authors. In the simulations by Visbal and Gordnier, time-averaged sub-vortices that co-rotate with the flow have also been observed. These authors postulate that they "are the imprint left by the regular break-up of the unsteady sub-structures" [70, p. 10]. The present simulations are consistent with this view.

6.2.2. Time averages for $\mathrm{Re_c} = 211,200$

Finally, some results of the simulation on the medium grid at the higher chord Reynolds number $\mathrm{Re_c} = 211,200$ are presented. Care should be taken in the interpretation of the results of this simulation, because the resolution of the medium grid may not be sufficient to accurately capture the shear layer at this higher chord Reynolds number. Fig. 20 shows axial slices of the time-averaged vorticity for local Reynolds numbers that correspond to a shear layer that is unsteady, but not fully turbulent.

The simulation at $\mathrm{Re_c} = 150,000$ predicts break-up of the time-averaged shear layer before $\mathrm{Re}_x = 100,000$. The simulation at $\mathrm{Re_c} = 211,200$ predicts break-up at a local Reynolds number between $\mathrm{Re}_x = 100,000$ and $\mathrm{Re}_x = 110,000$, which is somewhat higher than for $\mathrm{Re_c} = 150,00$. This is in agreement with the observation in Fig. 16 that the onset of the instability of the shear layer occurs at a higher local Reynolds number in the simulation at $\mathrm{Re_c} = 211,200$ than at $\mathrm{Re_c} = 150,000$.

7. Conclusions

We have presented accurate numerical simulations of transitional subsonic flow over a delta wing. The numerical method is fourth-order accurate and uses a skew-symmetric finite-volume discretization of the convective terms. In this way, the method discretely conserves the primary conserved quantities mass, momentum and total energy, but also the secondary conserved quantities kinetic and internal energy. As a result, artificial diffusion is not required to keep the simulations stable. The method has been implemented in the NLR simulation method Enflow.

The simulations indicate that the numerical method has good stability properties as a result of preserving the energy-conserving nature of the governing equations. It gives accurate results for the transitional aerodynamic flow over a delta wing studied experimentally by Riley and Lowson [56]. The primary challenge in these simulations is to accurately capture the development of the instability of the shear layer that separates at the leading edge of the wing [70,74]. Simulations have been performed at chord Reynolds numbers of $\mathrm{Re_c} = 150,000$ and $\mathrm{Re_c} = 211,200$. To study grid convergence, the simulations at the lower Reynolds number have been performed on coarse, medium, and fine grids. The numerical solution accurately converges to the fine grid solution above the delta wing. At the trailing edge of the wing, the numerical solution may not be fully converged, hence we think a classification as direct numerical simulation is not yet fully justified: some further refinement of the grid would be useful.

In the simulation at $\mathrm{Re_c} = 150,000$, unsteady counter-rotating sub-vortices are observed at the same axial location as in the experiment. Steady co-rotating sub-vortices which are observed in the experiments, are not observed in the simulations.

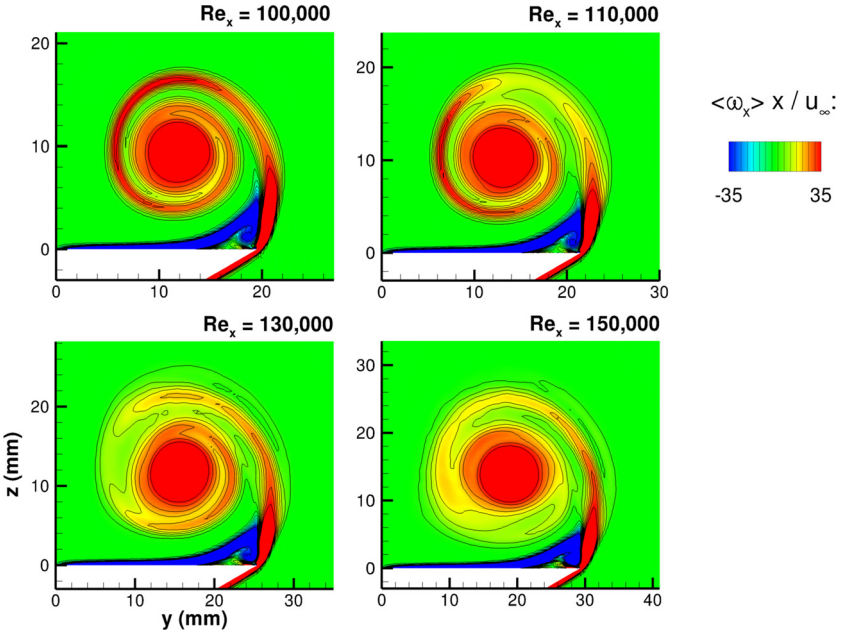

Fig. 20. Slices at several transitional axial local Reynolds numbers of the time-averaged axial vorticity scaled by the axial location $\langle\omega_x\rangle x/u_\infty$ for $\mathrm{Re_c} = 211,200$ as computed on the medium computational grid.

From physical experiments, it is known that the latter are masked by the unsteady sub-vortices which can be easily excited [73,56]. However, as in the experiments by Riley and Lowson [56] and the numerical simulations by Visbal and Gordnier [70], time-averaging of the unsteady counter-rotating sub-structures does give rise to steady co-rotating sub-structures. Possibly, both the steady and unsteady sub-vortices are physical, and the setup of an experiment or simulation determines which of the instabilities prevails.

As observed in the experiment, the simulations indicate that the development of the instantaneous shear layer is characterized by the local Reynolds number. At $\mathrm{Re_c} = 150,000$, the onset of unsteady flow and its transition to turbulence is accurately predicted, in good agreement with experimental data. Results of the simulation at $\mathrm{Re_c} = 211,200$ on the medium grid seem like a continuation of the simulation at $\mathrm{Re_c} = 150,000$, whereas in the experiments of Riley and Lowson [56], at the higher chord Reynolds number the onset of unsteady flow has moved downstream. Nevertheless, the onset of fully turbulent flow agrees closely with the experiments.

In conclusion, the numerical simulations performed with the fourth-order accurate energy-conserving method are numerically stable and the results accurately capture the transition to turbulence observed in the experiments. This demonstrates the practical applicability of low-dissipation methods for simulations of transitional flow over realistic aerodynamic objects.

Declaration of competing interest

The authors declare that they have no known competing financial interests or personal relationships that could have appeared to influence the work reported in this paper.

Acknowledgements

This research was supported by the Ubbo Emmius Fund of the University of Groningen. The research was carried out at the Bernoulli Institute for Mathematics, Computer Science and Artificial Intelligence of the University of Groningen, and the Flight Physics and Loads department of the Netherlands Aerospace Centre NLR. We acknowledge sponsoring by the Netherlands Organisation for Scientific Research (NWO) for the use of supercomputing facilities.

References

[1] S.B. Pope, Turbulent Flows, Cambridge University Press, 2000.
[2] P.A. Davidson, Turbulence: An Introduction for Scientists and Engineers, Oxford University Press, 2004.
[3] Haecheon Choi, Parviz Moin, Grid-point requirements for large-eddy simulation: Chapman's estimates revisited, Phys. Fluids 24 (2012) 011702, https://doi.org/10.1063/1.3676783.
[4] P. Beaudan, P. Moin, Numerical experiments on the flow past a circular cylinder at sub-critical Reynolds number, Technical report, Stanford University, 1994.
[5] A.G. Kravchenko, P. Moin, On the effect of numerical errors in large eddy simulations of turbulent flows, J. Comput. Phys. 131 (1997) 310–322.

[6] R. Mittal, P. Moin, Suitability of upwind-biased finite difference schemes for large-eddy simulation of turbulent flows, AIAA J. 35 (1997) 1415–1417.
[7] T. Colonius, S.K. Lele, Computational aeroacoustics: progress on nonlinear problems of sound generation, Prog. Aerosp. Sci. 40 (2004) 345–416.
[8] J.C. Kok, A high-order low-dispersion symmetry-preserving finite-volume method for compressible flow on curvilinear grids, J. Comput. Phys. 228 (2009) 6811–6832.
[9] Wybe Rozema, Roel W.C.P. Verstappen, Johan C. Kok, Arthur E.P. Veldman, Low-dissipation simulation methods and models for turbulent subsonic flow, Arch. Comput. Methods Eng. (2019).
[10] N.A. Phillips, The general circulation of the atmosphere: a numerical experiment, Q. J. R. Meteorol. Soc. 82 (1956) 123–164.
[11] N.A. Phillips, An example of non-linear computational instability, in: The Atmosphere and the Sea in Motion, The Rockefeller Institute Press, 1959, pp. 501–504.
[12] Douglas K. Lilly, On the computational stability of numerical solutions of time-dependent non-linear geophysical fluid dynamics problems, Mon. Weather Rev. 93 (1) (1965) 11–26.
[13] A. Arakawa, Computational design for long-term numerical integration of the equations of fluid motion: two-dimensional incompressible flow. Part I, J. Comput. Phys. 1 (1966) 119–143.
[14] Kirk Bryan, A scheme for numerical integration of the equations of motion on an irregular grid free of nonlinear instability, Mon. Weather Rev. 94 (1) (1966) 38–40.
[15] F.H. Harlow, J.E. Welch, Numerical calculation of time-dependent viscous incompressible flow of fluid with free surface, Phys. Fluids 8 (1965) 2182–2189.
[16] R.D. Richtmyer, K.W. Morton, Difference Methods for Initial-Value Problems, 2nd edition, John Wiley & Sons, New York, 1967.
[17] S.A. Piacsek, G.P. Williams, Conservation properties of convection difference schemes, J. Comput. Phys. 6 (1970) 392–405.
[18] Y. Morinishi, T.S. Lund, O.V. Vasilyev, P. Moin, Fully conservative higher order finite difference schemes for incompressible flow, J. Comput. Phys. 143 (1998) 90–124.
[19] O.V. Vasilyev, High order difference schemes on non-uniform meshes with good conservation properties, J. Comput. Phys. 157 (2000) 746–761.
[20] F.E. Ham, F.S. Lien, A.B. Strong, A fully conservative second-order finite difference scheme for incompressible flow on nonuniform grids, J. Comput. Phys. 177 (1) (2002) 117–133.
[21] A.E.P. Veldman, K. Rinzema, Playing with nonuniform grids, J. Eng. Math. 26 (1991) 119–130.
[22] R.W.C.P. Verstappen, A.E.P. Veldman, Direct numerical simulation of turbulence at lesser costs, J. Eng. Math. 32 (1997) 143–159.
[23] R.W.C.P. Verstappen, A.E.P. Veldman, Spectro-consistent discretization of Navier-Stokes: a challenge to RANS and LES, J. Eng. Math. 34 (1998) 163–179.
[24] R.W.C.P. Verstappen, A.E.P. Veldman, Symmetry-preserving discretization of turbulent flow, J. Comput. Phys. 187 (2003) 3670–3681.
[25] X. Trias, M. Soria, A. Oliva, R. Verstappen, Regularization models for the simulation of turbulence in a differentially heated cavity, in: P. Wesseling, E. Oñate, J. Periaux (Eds.), Proc. Europ. Conf. Comput. Fluid Dyn.: ECCOMAS CFD 06, Egmond aan Zee, ISBN 909020970-0, 2006 (CD-ROM) paper 88.
[26] F.X. Trias, O. Lehmkuhl, A. Oliva, C.D. Pérez-Segarra, R.W.C.P. Verstappen, Symmetry-preserving discretization of Navier-Stokes equations on collocated unstructured grids, J. Comput. Phys. 258 (2014) 246–267.
[27] Lluís Jofre, Oriol Lehmkuhl, Jordi Ventosa, F. Xavier Trias, Assensi Oliva, Conservation properties of unstructured finite-volume mesh schemes for the Navier–Stokes equations, Numer. Heat Transf., Part B, Fundam. 65 (1) (2014) 53–79.
[28] Eugenio Schillaci, Lluís Jofre, Néstor Balcázar, Oscar Antepara, Assensi Oliva, A low-dissipation convection scheme for the stable discretization of turbulent interfacial flow, Comput. Fluids 153 (2017) 102–117.
[29] B. Strand, Summation by parts for finite difference approximations for d/dx, J. Comput. Phys. 110 (1994) 47–67.
[30] Pelle Olsson, Summation by parts, projections, and stability, I, Math. Comput. 64 (211) (1995) 1035–1065.
[31] Pelle Olsson, Summation by parts, projections, and stability, II, Math. Comput. 64 (212) (1995) 1473–1493.
[32] Ken Mattsson, Jan Nordström, Summation by parts operators for finite difference approximations of second derivatives, J. Comput. Phys. 199 (2) (2004) 503–540.
[33] Magnus Svärd, Ken Mattsson, Jan Nordström, Steady-state computations using summation-by-parts operators, J. Sci. Comput. 24 (1) (2005) 79–95.
[34] Svärd Magnus, Jan Nordström, Review of summation-by-parts schemes for initial–boundary-value problems, J. Comput. Phys. 268 (2014) 17–38.
[35] W.J. Feiereisen, W.C. Reynolds, J.H. Ferziger, Numerical simulation of a compressible, homogeneous, turbulent shear flow, Report TF-13, Thermosciences Division, Mechanical Engineering, Stanford University, 1981.
[36] G.A. Blaisdell, N.N. Mansour, W.C. Reynolds, Numerical simulations of compressible homogeneous turbulence, Report TF-50, Thermosciences Division, Mechanical Engineering, Stanford University, 1991.
[37] F. Ducros, F. Laporte, T. Souleres, V. Guinot, P. Moinat, B. Caruelle, High-order fluxes for conservative skew-symmetric-like schemes in structured meshes: application to compressible flows, J. Comput. Phys. 161 (1) (2000) 114–139.
[38] A. Jameson, Formulation of kinetic energy preserving conservative schemes for gas dynamics and direct numerical simulation of one-dimensional viscous compressible flow in a shock tube using entropy and kinetic energy preserving schemes, J. Sci. Comput. 34 (2008) 188–208.
[39] J. Nordström, J. Gong, E. van der Weide, M. Svärd, A stable and conservative high order multi-block method for the compressible Navier–Stokes equations, J. Comput. Phys. 228 (24) (2009) 9020–9035.
[40] Y. Morinishi, Skew-symmetric form of convective terms and fully conservative finite difference schemes for variable density low-Mach number flows, J. Comput. Phys. 229 (2010) 276–300.
[41] W. Rozema, J.C. Kok, R.W.C.P. Verstappen, A.E.P. Veldman, A symmetry-preserving discretisation and regularisation model for compressible flow with application to turbulent channel flow, J. Turbul. 15 (6) (2014) 386–410.
[42] B. van't Hof, A.E.P. Veldman, Mass, momentum and energy conserving (MaMEC) discretizations on general grids for the compressible Euler and shallow water equations, J. Comput. Phys. 231 (2012) 4723–4744.
[43] G. Coppola, F. Capuano, L. de Luca, Discrete energy-conservation properties in the numerical solution of the Navier–Stokes equations, Appl. Mech. Rev. 71 (2019) 010803.
[44] J.-L. Guermond, L. Quartapelle, A projection FEM for variable density incompressible flows, J. Comput. Phys. 165 (2000) 167–188.
[45] P.K. Subbareddy, G.V. Candler, A fully discrete, kinetic energy consistent finite-volume scheme for compressible flows, J. Comput. Phys. 228 (2009) 1347–1364.
[46] W. Rozema, H.J. Bae, P. Moin, R. Verstappen, Minimum-dissipation models for large-eddy simulation, Phys. Fluids 27 (2015) 085107.
[47] J. Reiss, J. Sesterhenn, A conservative, skew-symmetric finite difference scheme for the compressible Navier-Stokes equations, Comput. Fluids 101 (2014) 208–219.
[48] J. Brouwer, J. Reiss, J. Sesterhenn, Conservative time integrators of arbitrary order for skew-symmetric finite-difference discretizations of compressible flow, Comput. Fluids 100 (2014) 1–12.
[49] J. Reiss, A family of energy stable, skew-symmetric finite difference schemes on collocated grids, J. Sci. Comput. 65 (2015) 1–18.
[50] W. Rozema, J.C. Kok, R.W.C.P. Verstappen, A.E.P. Veldman, A symmetry-preserving discretization and regularization model for compressible flow, in: Eighth International Symposium on Turbulence and Shear Flow Phenomena (TSFP8), 2013, p. COMP2E.
[51] W. Rozema, R.W.C.P. Verstappen, J.C. Kok, A.E.P. Veldman, Discretizations and regularization models for compressible flow that preserve the skew-symmetry of convective transport, in: 6th European Conference on Computational Fluid Dynamics (ECFD VI), 2014.

[52] W. Rozema, Low-dissipation methods and models for the simulation of turbulent subsonic flow, PhD thesis, University of Groningen, 2015.
[53] Francois Cadieux, Michael Barad, Cetin Kiris, A high-order kinetic energy conserving scheme for compressible large-eddy simulation, in: Proc. 10th Int. Conf. Comp. Fluid Dyn. ICCFD10, Barcelona, July 9-13 2018, paper ICCFD10-2018-100.
[54] W. Rozema, R.W.C.P. Verstappen, J.C. Kok, A.E.P. Veldman, A symmetry-preserving discretization and regularization subgrid model for compressible turbulent flow, in: Direct and Large-Eddy Simulation IX, Springer International Publishing, 2015, pp. 319–325.
[55] W. Rozema, J.C. Kok, R.W.C.P. Verstappen, A.E.P. Veldman, DNS and LES of the compressible flow over a delta wing with the symmetry-preserving discretization, in: ASME 2014 4th Joint US-European Fluids Engineering Division Summer Meeting Collocated With the ASME 2014 12th International Conference on Nanochannels, Microchannels, and Minichannels, American Society of Mechanical Engineers, 2014, FEDSM2014-21374.
[56] A.J. Riley, M.V. Lowson, Development of a three-dimensional free shear layer, J. Fluid Mech. 369 (1998) 49–88.
[57] Peter J. Olver, A nonlinear Hamiltonian structure for the Euler equations, J. Math. Anal. Appl. 89 (1) (1982) 233–250.
[58] J.C. Kok, H. van der Ven, Capturing free shear layers in hybrid RANS-LES simulations of separated flow, Technical Report NLR-TP-2012-333, National Aerospace Laboratory NLR, 2012.
[59] J.C. Kok, H. van der Ven, E. Tangermann, S. Sanchi, A. Probst, K.A. Weinman, L. Temmerman, Vortex breakdown above a delta wing with sharp leading edge, 2015, Application Challenge AC1-09, ERCOFTAC QNET-CFD Wiki.
[60] Marcel Vinokur, Conservation equations of gasdynamics in curvilinear coordinate systems, J. Comput. Phys. 14 (2) (1974) 105–125.
[61] Marcel Vinokur, An analysis of finite-difference and finite-volume formulations of conservation laws, J. Comput. Phys. 81 (1) (1989) 1–52.
[62] Arthur E.P. Veldman, A general condition for kinetic-energy preserving discretization of flow transport equations, J. Comput. Phys. (2019), in print, doi.org/10.1016/j.jcp.2019.108894.
[63] C.K.W. Tam, J.C. Webb, Dispersion-relation-preserving finite difference schemes for computational acoustics, J. Comput. Phys. 107 (1993) 262–281.
[64] L. Eça, M. Hoekstra, Evaluation of numerical error estimation based on grid refinement studies with the method of the manufactured solutions, Comput. Fluids 38 (8) (2009) 1580–1591.
[65] O. Lucca-Negro, T. O'Doherty, Vortex breakdown: a review, Prog. Energy Combust. Sci. 27 (2001) 431–481.
[66] A.M. Mitchell, J. Délery, Research into vortex breakdown control, Prog. Aerosp. Sci. 37 (2001) 385–418.
[67] J.D. Anderson, Fundamentals of Aerodynamics, McGraw-Hill, Inc., 1984.
[68] M. Gad-el-Hak, R.F. Blackwelder, The discrete vortices from a delta wing, AIAA J. 23 (1985) 961–962.
[69] R.E. Gordnier, M.R. Visbal, Unsteady vortex structure over a delta wing, J. Aircr. 31 (1994) 234–248.
[70] M.R. Visbal, R.E. Gordnier, On the structure of the shear layer emanating from a swept leading edge at angle of attack, in: 33rd AIAA Fluid Dynamics Conference and Exhibit, 2003, paper AIAA 2003-4016.
[71] F.M. Payne, T.T. Ng, R.C. Nelson, L.B. Schiff, Visualization and wake surveys of vortical flow over a delta wing, AIAA J. 26 (1988) 137–143.
[72] A.E. Washburn, K.D. Visser, Evolution of vortical structures in the shear layer of delta wings, in: 25th AIAA Fluid Dynamics Conference, 1994, paper AIAA-94-2317.
[73] G.A. Reynolds, A.A. Abtahi, Three-dimensional vortex development breakdown, and control, in: AIAA 2nd Shear Flow Conference, 1989, paper AIAA-89-0998.
[74] A.M. Mitchell, S.A. Morton, J.R. Forsythe, R.M. Cummings, Analysis of delta-wing vortical substructures using detached-eddy simulation, AIAA J. 44 (2006) 964–972.
[75] M. Lesieur, Turbulence in Fluids, Kluwer Academic Publishers, 1997.